Embedded Magnetic Sensing for Feedback Control of Soft HASEL Actuators

Vani Sundaram, Khoi Ly, Brian K. Johnson, Mantas Naris, Maxwell P. Anderson, James Sean Humbert, Nikolaus Correll, *Senior Member, IEEE*, and Mark Rentschler, *Senior Member, IEEE*

***Abstract*— The need to create more viable soft sensors is increasing in tandem with the growing interest in soft robots. Several sensing methods, like capacitive stretch sensing and intrinsic capacitive self-sensing, have proven to be useful when controlling soft electro-hydraulic actuators, but are still problematic. This is due to challenges around high-voltage electronic interference or the inability to accurately sense the actuator at higher actuation frequencies. These issues are compounded when trying to sense and control the movement of a multiactuator system. To address these shortcomings, we describe a two-part magnetic sensing mechanism to measure the changes in displacement of an electro-hydraulic (HASEL) actuator. Our magnetic sensing mechanism can achieve high accuracy and precision for the HASEL actuator displacement range, and accurately tracks motion at actuation frequencies up to 30 Hz, while being robust to changes in ambient temperature and relative humidity. The high accuracy of the magnetic sensing mechanism is also further emphasized in the gripper demonstration. Using this sensing mechanism, we can detect submillimeter difference in the diameters of three tomatoes. Finally, we successfully perform closed-loop control of one folded HASEL actuator using the sensor, which is then scaled into a deformable tilting platform of six units (one HASEL actuator and one sensor) that control a desired end effector position in 3D space. This work demonstrates the first instance of sensing electro-hydraulic deformation using a magnetic sensing mechanism. The ability to more accurately and precisely sense and control HASEL actuators and similar soft actuators is necessary to improve the abilities of soft, robotic platforms.**

***Index Terms*—Electrohydraulic actuators, feedback control, magnetic-based sensors, soft robotics, soft sensors.**

Manuscript received 20 March 2022; revised 16 July 2022; accepted 26 July 2022. This work was supported by the National Science Foundation Graduate Research Fellowship Program under Grand DGE 1650115. This article was recommended for publication by Associate Editor H. Zhao and Editor M. Yim upon evaluation of the reviewers' comments. *(Corresponding author: Vani Sundaram.)*

Vani Sundaram, Brian K. Johnson, Mantas Naris, Maxwell P. Anderson, James Sean Humbert, and Mark Rentschler are with the Department of Mechanical Engineering, University of Colorado Boulder, Boulder, CO 80309 USA (e-mail: vani.sundaram@colorado.edu; brian.k.johnson@colorado.edu; mantas.naris@colorado.edu; maxwell.anderson@colorado.edu; sean.humbert@colorado.edu; mark.rentschler@colorado.edu).

Khoi Ly is with the Sibley School of Mechanical and Aerospace Engineering, Cornell University, Ithaca, NY 14853 USA (e-mail: kdl54@cornell.edu).

Nikolaus Correll is with the Department of Computer Science, University of Colorado Boulder, Boulder, CO 80309 USA, and also with the Materials Science and Engineering Program, University of Colorado Boulder, Boulder, CO 80309 USA (e-mail: nikolaus.correll@colorado.edu).

This article has supplementary material provided by the authors and color versions of one or more figures available at https://doi.org/10.1109/TRO.2022.3200164.

Digital Object Identifier 10.1109/TRO.2022.3200164

I. Introduction

SOFT robotics is a field of robotic system design characterized by physically flexible bodies with rich functionalities that are similar to those found in living organisms. The integration of soft actuators, soft sensors, and interfacing electronics allows these robots to not only mimic the performance of biological systems, but also provide advantages that conventional, rigid robots are inherently incapable of, such as adaptability in unstructured environments [1], [2], [3], [4]. These advantages have generated substantial interest in using soft robots for rehabilitation and wearable devices [5], [6], [7], [8], prosthetics and orthotics [9], [10], implantable devices and surgical tools [11], [12], [13], manufacturing applications [14], [15], and search-and-rescue technology [1], [16]. Over the past few decades, several methods of actuation have come to fruition, including electrostatic [17], [18], [19], hydraulic and microhydraulic [6], [20], [21], pneumatic [22], [23], [24], magnetic and electromagnetic [25], [26], [27], [28], shape memory alloy based actuation [29], [30], and electro-hydraulic (HASEL) actuators [31]. Relatively high actuation frequency, large strains, significant peak specific power, and ease of manufacturing [32], [33], [34] are some of the distinct advantages of HASEL actuators over other soft actuators.

Due to their deformable and compliant nature, state estimation in such actuators using embedded and distributed sensing has been a necessary, ongoing challenge [35], [36], [37], [38], [39]. Integrating a reliable sensing mechanism with the actuation method is necessary for the robot to interact with its environment. Soft actuators require compatible embedded sensors that are sufficiently fast for feedback control, but do not restrict the actuators' high-speed dynamics. To address this design goal, specifically for HASEL actuators, there are a number of works focusing on integrating sensors for feedback control, including a laser position sensor [37], capacitive self-sensing method [40], [41], and a capacitive soft strain sensor [37]. While these previously used sensing mechanisms are sufficient for feedback control of electrohydraulic actuators, they each present several problems. Expensive, bulky, benchtop sensors such as laser position sensors are only useful in a stationary environment, whereas capacitive stretch sensor and the capacitive self-sensing circuit are currently limited by low sensing rates and resolutions, and relatively complex designs and manufacturing processes. Specifically, the capacitive stretch sensor is prone to electric field noise generated by the actuator and arcing when high voltage is applied to the actuator.

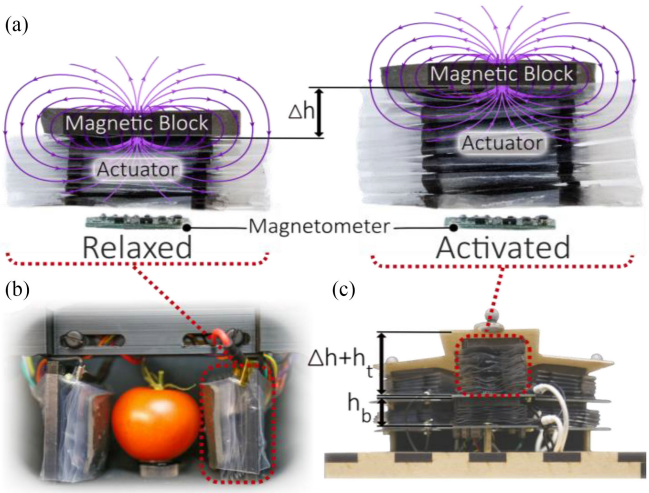

Fig. 1. (a) One unit includes the magnetic sensing mechanism (composed of the magnetometer and soft magnetic block) used to measure the change in height, Δh, and a folded HASEL actuator that is sandwiched in between. The figure exaggerates the distance between the actuator and the magnetometer for clarity purposes; in reality, the actuator sits directly on top of the magnetometer. (b) Two-finger gripper contains 2-units shown in (a), which are used to determine the diameter of objects like a tomato. (c) 6-unit deformable robotic platform has two layers. Each layer is comprised of three of the units shown in (a). The height of the top layer h_t is measured relative to the base of the top layer. The bottom layer height h_b is relative to the stationary base. In both (b) and (c), the magnetometers for each unit are flush with the base of the actuator, so they are not visible in these images.

To address some of the shortcomings of existing sensing methods used for electrohydraulic actuators, such as HASEL actuators, we propose the use of a magnet-based sensing method to measure the change in shape of a soft actuator. Specifically, we focus on measuring the linear displacement of a folded HASEL actuator. This sensing method is composed of a magnetic silicone block that is placed on top of a folded HASEL actuator [Fig. 1(a)]. As the actuator moves, an off-the-shelf magnetometer, placed under the actuator, registers the change in magnetic flux density of the magnetic block.

A. Related Soft, Magnetic Sensing Mechanisms in Literature

The concept of magnetic-based sensing is enticing for robotic systems that require highly accurate and fast sensor information [42]. The first tactile sensor utilizing a magnetic component and a magnetic sensor appeared in Clark et al.'s [43] published work in 1988. Several studies since then have used a magnetic sensing mechanism to receive tactile feedback in devices such as robotic fingertips. Paulino et al. [44] integrated four 3-axis hall-effect sensors paired with four magnets embedded in the elastomer-coated fingertips of a robot, allowing the robot to sense both normal and shear forces. Bin Rosle et al. [45] used multiple magnets and one 3-axis hall-effect sensor to determine the deformation and orientation of a robotic gripper. The use of tactile magnetic sensors can also allow for classification of different objects [46], [47].

To create an entirely soft tactile sensor, some magnetic sensing mechanisms substitute rigid magnets with a magnetic, soft substrate [48], [49], [50], [51], [52], [53]. Using a soft substrate with embedded magnetic particles of high intrinsic coercivity can improve the durability of the material compared with embedding hard, rigid magnets in a soft material [49]. Using a soft magnetic substrate allows for any type of shape or thickness, depending on the distance between the sensor and the magnetic material. This simplifies the fabrication process when modifying the magnetic component. Also, by using a soft substrate for the magnetic component, we can handle delicate objects, like a tomato, without damaging them.

Besides tactile sensing, the change in magnetic flux density can also be used to determine joint angle of a single joint arm [54], proximity of a magnetic skin to a magnetic sensor [50], and curvature of a soft, bidirectional bending pneumatic actuator [51]. While magnetic sensing has been explored in many different areas of soft robotics, none of the applications are applied to electrostatic soft actuators. Here, we demonstrate the first example of sensing the change in deformation of a soft, electrostatic actuator in between the magnetic sensor and the magnetic component. We use techniques similar to Hellebrekers et al. [49], but our system uses the magnetic components to relate a change in actuator stroke to a change in magnetic flux density instead of sensing external forces on a magnetic surface. Using a magnetic block for each actuator allows for easy mapping procedures to get measured displacement from sensed magnetic flux density. It also allows for a modular design when scaling up to larger robotic systems, like the multiunit robotic platform described in this work.

B. Contribution of This Work and Article Outline

To the best of our knowledge, this work is the first to demonstrate the use of magnetic sensing for estimating shape changes of soft electrostatic actuators. While this method can theoretically be used for any actuator that does not generate an interfering magnetic field (often due to high current usage), we specifically focus on folded HASEL actuators, which operate on high voltage and low current. This straightforward sensing mechanism exhibits excellent performance compared with previous on-board sensors used for folded HASEL actuators (see Section IV-C). By sandwiching the actuator between an off-the-shelf magnetometer and a magnetic component, [see Fig. 1(a)], we can map changes in the sensed magnetic flux density to changes in the actuator shape at high HASEL actuation frequencies (30 Hz) at a precision with a standard deviation of measurement less than 0.15 mm. To show the submillimeter accuracy, we measure the diameter of multiple tomatoes with similar measurements and compare the sensor output to a caliper reading. We also demonstrate a potential application of this magnetic sensing approach by precisely controlling the heights of six HASEL actuators, effectively moving the end effector of the two-segment, HASEL-based robotic platform, referred to as the deformable platform, shown in Fig. 1(b) and (c). Acknowledging that the magnetic sensing mechanism is a two-part mechanism requiring a magnetometer and a magnetic block, we will henceforth refer to this mechanism as the sensor. We will also refer to the combination of the sensor with a folded

HASEL actuator as a unit. Section II introduces the hardware needed to create the sensor and the manufacturing methods for the magnetic block. It also breaks down the components of the magnetometer circuit and the fabrication process of the folded HASEL actuator. Section III describes the experimental setup and results of the tests to quantify the range, accuracy, and precision of the sensor, along with the mapping of magnetic flux density (mG) to change in height (mm). Section IV explains the mapping validation method using the folded HASEL actuator, highlights the open-loop demonstration of the two-finger gripper showing high accuracy, and compares the performance of the sensor to a capacitive stretch sensor. Section V explains the dynamics of the closed-loop system for a single unit. Section VI describes the deformable platform setup, circuity, and the experimental procedure, and Section VII provides the deformable platform demonstration results, which support the effectiveness of using this sensor to control multiple folded HASEL actuators. Lastly, Section VIII summarizes the results and novelty of this work and concludes this article.

II. Magnetic Sensing Hardware and Manufacturing

A. Magnetic Block Manufacturing Process

We based the fabrication process of the magnetic silicone blocks on Hellebrekers et al.'s [49] manufacturing procedure. The magnetic components of the sensing mechanism are flexible, silicone blocks (Ecoflex 00–30, Smooth On) suffused with bonded neo-powder (NQP-B+ 20441, Neo Magnequench). First, we hand mixed the Ecoflex Parts A and B rubbers using a 1:1 weight ratio. After mixing the silicone for approximately 30 s, we manually mixed in 1.67 weight (w.t.) % of neo-powder. Once most of the powder was roughly distributed in the silicone, we placed the mixture into a planetary mixer (ARV-310, Thinky). The mixture was first degassed in a vacuum (∼0.2 kPa) for 60 s, then mixed at a speed of 2000 rpm for 30 s, before the speed decreased to 200 rpm at 10.5 kPa for 60 s.

After the mixing and degassing process was complete, the powder was fully shear-mixed into the silicone, which is shown in Fig. 2(b) using an electron microscope (Xradia 520 Versa, Zeiss). We poured the mixture into a 50 mm × 50 mm × 5 mm acrylic mold; a 5 mm thickness was chosen to level the change in height of the foldable HASEL, creating a more even stroke.

We then filled the mixture in the mold and placed it in the center of the empty volume between two ND42 4 in × 4 in × 1 in magnets (CMS Magnetics) separated by 4 cm. The mixture was cured for about 2.5 h before being removed from the acrylic mold. This process polarizes the magnetic particles in the mixture as the silicone cures, creating an N-S orientation [see Fig. 2(a)]. If the magnetic mixture is cured without the magnetic polarization process, the cured block's magnetic field will be negligible compared to that of the block cured in between the ND42 magnets [see Fig. 2(c)]. The magnetic flux density of six blocks was measured using a fully calibrated magnetometer, resulting in an average strength of 8632 ± 73 mG. The average weight of the blocks was 10.6 ± 0.6 g.

Commercial, hard NdFeB magnets can significantly improve the sensing range, accuracy, and precision because the fabricated

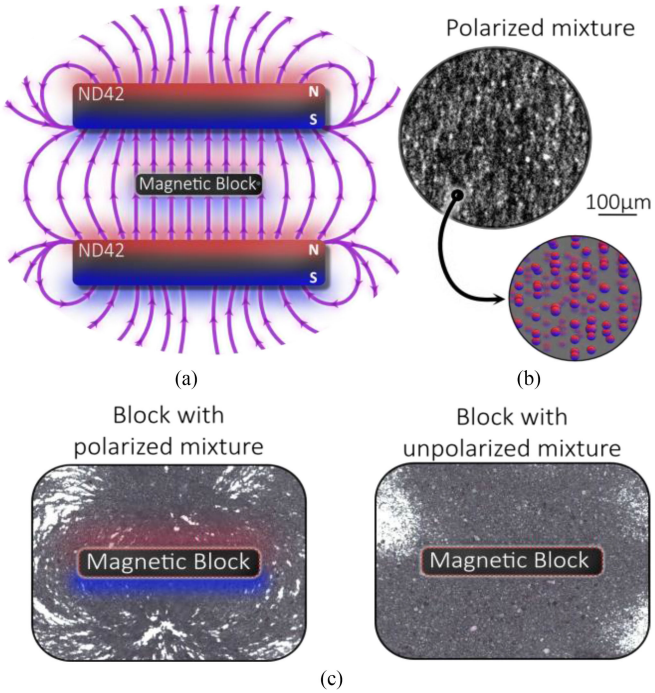

Fig. 2. (a) To define the soft magnetic block's magnetic field orientation, a silicone and NdFeB powder mixture was placed in between two 4 in × 4 in × 4 in Neodymium −42 (ND42) magnets while curing. (b) Image using an electron microscope and cartoon schematic of the isotropic distribution of magnetic particles in the soft substrate. (c) When the magnetic block cures in the setup shown in (a), the mixture becomes polarized and retains a baseline remanence magnetization. When the block is placed under a layer of iron fillings, the fillings align with the magnetic field produced by the block, shown in the left image. When the block is not polarized during the curing process, the fillings are unaffected, as shown in the right image.

soft magnets do not have the same density of magnetic powder. However, embedding a hard magnet on soft HASEL actuators takes away the intrinsic compliance of the actuators that are useful for many robotic applications, such as grasping objects (hard or soft), due to improved area of contact and conformity to the objects.

B. Magnetic Sensing Circuit

We use a low cost, off-the-shelf 3-axis magnetometer (LIS3MDL, ST Electronics) on a breakout board (LIS3MDL Carrier, Pololu) to sense the change of the magnetic flux density as the magnetic block moves. We use a microcontroller unit, or MCU, (Teensy 3.6, PJRC) to receive digital data of the raw magnetic flux density from the sensor via a four-wire SPI communication protocol at a selectable resolution, range, and sampling rate up to 1 kHz. The magnetic block covers the top of an actuator of interest, and both are placed on top of a magnetometer [Fig. 1(a)]. This configuration allows us to measure the change in magnetic flux density as the distance between the block and the sensor varies due to the displacement of the actuator. To simplify the sensing problem, the x- and y-sensing axes of the magnetometer were disabled, and only the z-axis, which is parallel to the direction of travel of the magnetic block, was used. The SPI clock speed was set to 2 MHz using

SPI Mode 0. Since we were only looking at the magnetic flux density in one-dimension, no further calibration or additional algorithm was required to initialize and set up the sensor.

C. Fabrication Process of a Folded HASEL Actuator

The method of creating the folded HASEL actuators in this work is similar to that described in Mitchell et al. [33]. The folded HASEL stack is composed of twelve actuator pouches folded on top of each other to create a positive z-stroke when the pouches deform under an applied voltage. Two layers of 20-µm thick polyester lidding film (L0WS, Multiplastics) were heat-sealed together using a modified CNC machine (Shapeoko 3XL, Carbide 3D) to create a line of the individual actuator pouches. We then screen-printed a thin flexible layer of conductive ink (CI-2051, Engineered Materials System) on both sides of sealed film before filling the pouches with a silicone liquid dielectric (PSF-5cSt, Clearco). Once filled and fully sealed using a soldering iron (WE1010NA, Weller), we folded the string of actuator pouches using an accordion fold and secured the stack using thin strips of transfer tape (924, 3M). The lower viscosity dielectric liquid was used to improve the rise and fall times of the actuator compared with the previous folded HASEL actuator [55].

III. Sensing Range, Accuracy, and Precision

A. Experimental Setup for Characterization of the Sensor

We were keen on understanding how the accuracy and precision changes as a function of distance between the magnetometer and the magnetic block beyond the folded HASEL actuator's displacement range. This information describes how these two parameters change for other actuators with varying maximum heights, given this specific magnetic block. Therefore, we designed a fully mechanical stand to change the distance d (mm) between the sensor and the block at submillimeter increments.

The setup, represented in Fig. 3(a), was composed of 3D printed polymer materials, acrylic sheets, aluminum, and stainless-steel components to prevent distortion to the registered magnetic flux density. The magnetic block was placed on a laser-cut acrylic sheet attached to an aluminum block, which moved vertically along a stainless-steel 2 mm pitch T8 lead screw. Two pillow block bearings supported the lead screw to minimize any horizontal movement as the magnetic block moved along the screw. To move the magnetic block at 0.1 mm with every full rotation, we implemented a 3D printed three-gear system with a 20:1 turn ratio attached to a manual hand crank.

A magnetometer was mounted directly below the center of the magnetic block and the data was read by an MCU. We used a commercial laser position sensor (LK-H157, Keyence) to track the movement of the magnetic block and measure the change in distance between the magnetic block and magnetometer. The output voltage of the laser position sensor was sent through a 12-b ADC. We sampled the magnetometer data B_z (mG) and the laser position sensor d_{laser} (mm) at 1 kHz via serial communication.

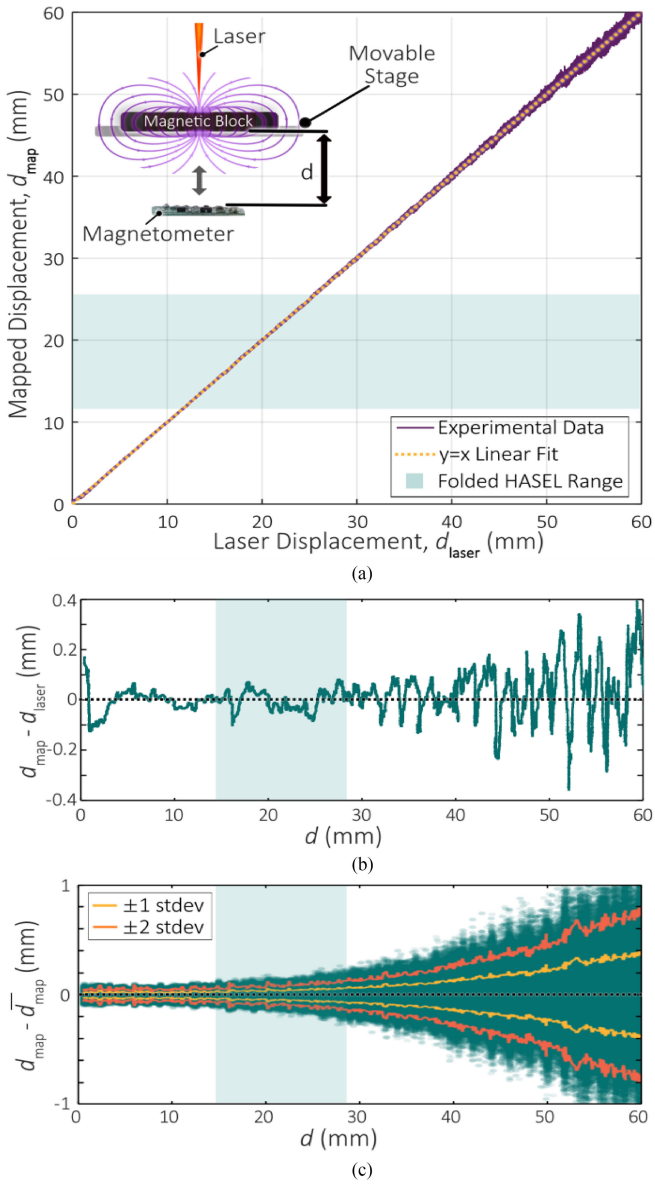

Fig. 3. (a) Data from the laser position sensor d_{laser} and the mapped displacements d_{map}, calculated using (1), from the changes in magnetic field strength closely align with the linear $y = x$ fit ($R^2 = 0.9959$), which is represented by the dotted line. The right y-axis shows the changes in resolution as the distance d between the sensor and magnetic block increases. The faded, rectangular section highlights the displacement range (11–23 mm) of a folded HASEL. (b) Accuracy is computed from the deviation of the measured value d_{map} to the ground-truth value d_{laser}. The accuracy in the displacement range of the HASEL is ±0.1 mm. (c) Precision, or the difference between d_{map} and a moving average mean with a nonoverlapping window of 5000 data points, $\bar{d}_{map}$, decreases as a function of displacement due to the inverse cubic relationship between displacement and magnetic flux density. The precision within the displacement range of the HASEL is ±0.15 mm.

B. Mapping of Magnetometer Raw Output Data to Actuator's Displacement

We conducted five trials of moving the magnetic block from 0 to 25 mm away from the magnetometer at 0.05 mm increments, which covers the range of the folded HASEL actuator. We then conducted five more tests moving the block at 0.1 mm increments from 2 to 60 mm. We held the displacement for a

few seconds between each incremental increase. The magnetic flux density along the z-axis was mapped to the change in vertical distance using a least squares polynomial curve fitting function (MATLAB R2020a). Based on magnetostatic theory, we reasoned that the magnetic flux density would have a cubic relationship with the change in distance [56]. The resulting third-degree polynomial was

$$\begin{aligned} d_{\text{map}} &= p_3 \times B_{\text{z}}^3 + p_2 \times B_{\text{z}}^2 + p_1 \times B_{\text{z}} + p_0 \\ p_3 &= -9.332 \times 10^{-10} \quad p_2 = 1.041 \times 10^{-5} \\ p_1 &= -0.044 \qquad\qquad p_0 = 85.618 \end{aligned} \tag{1}$$

where d_{map} is the displacement of the block relative to the magnetometer in mm and B_{z} is the change in magnetic flux density along the z-axis in mG. Fitting this polynomial to obtain displacement data from the magnetometer data resulted in an excellent R-squared value of 0.9959. Fig. 3(a) shows the comparison between the laser displacement data d_{laser} with the mapped displacement data d_{map} based on the magnetometer output from all ten trials. We computed the accuracy [see Fig. 3(b)] and precision [see Fig. 3(c)] of the sensing mechanism from 0–60 mm. The accuracy compares the ground-truth data, d_{laser}, with our measured data, d_{map}; Fig. 3(b) shows a slight decrease in accuracy as the displacement d increases. To calculate precision, we compared d_{map} to the means of the measured displacement holds $\bar{d}_{\text{map}}$ during each test. These quasistatic means $\bar{d}_{\text{map}}$ were computed as the moving average mean with a nonoverlapping window of 5,000 data points. The precision degrades as the displacement d increases, since the magnetic flux density has an inverse cubic relationship with distance. However, the decrease in accuracy and precision can be addressed by increasing the magnetic flux density from the magnetic block by changing the concentration of magnetic particles or increasing the strength of the magnetic field used during the curing process mentioned in Section II-A.

The baseline height of a folded HASEL actuator is approximately 11 mm, which determines the baseline gap between the magnetic block and the magnetometer. As the actuator height increases to its maximum height due to increasing applied high voltage, the distance between the magnetic block and the magnetometer subsequently increases to a maximum distance of approximately 23 mm. Within the vertical range of the folded HASEL actuator, we can reliably expect a high accuracy with error between measurement and ground truth data less than ± 0.1 mm and precision with deviation bounds within ± 0.15 mm [see Fig. 3(b) and(c)], which is suitable to track the movement of a folded HASEL actuator.

IV. Mapping Validation

A. Validating the Sensing System Using an Actuator

HASEL actuators operate at high voltage but low current in the milliampere range [33], so we expected the reading of the sensor to be unaffected by the interfering magnetic field generated by the current driving the folded HASEL actuator. To verify this claim, we sandwiched a folded HASEL actuator with a magnetic block and the magnetometer, creating a unit [see Fig. 4(a)], and used (1) to map B_{z} to d. A $<$100-μm silicone sheet was wrapped around the magnetic block and the actuator to prevent the block from shifting off the top of the actuator as it moved at high frequencies. The input voltage to the actuator was sent through a waveform generator (33509B, KEYSIGHT) to a high-voltage amplifier (50/12, TREK), which was attached to the electrodes of the actuator.

Existing soft sensors are often affected by the change of environmental parameters, such as temperature and humidity [57]. We demonstrate that changes in the environment's temperature and humidity do not affect the readings from this sensor. We performed a series of nine tests in different environmental conditions; the ambient temperature and relative humidity were measured using a low-power humidity and temperature sensor evaluation board (HDC1080EVM, Texas Instruments). Using permutations of table fans, heat guns, and humidifiers, we varied the temperature between 18°C and 56°C and the relative humidity between 3.1% and 53.2%.

The input voltages were defined by 4 kV offset sine waves with a 4 kV amplitude and frequencies that ranged from 0.01 to 30 Hz. The laser displacement data and the magnetic flux density data were sampled at 1 kHz using an MCU, which sent data to a computer via serial communication. The TREK was turned OFF between each test to prevent the charge retention in the HASEL from compounding, effectively limiting the maximum stroke of the actuator. The laser position sensor probed the center of the magnetic block to record the true actuator height.

Five cycles from each of the nine tests were analyzed for each frequency, equating to forty-five cycles for each of the fourteen frequencies that we tested. The magnetic sensing method accurately monitors the movement of the actuator, even at larger actuation frequencies (30 Hz), when the HASEL barely moves. Fig. 4 shows the comparison of the laser position data and the mapped magnetic sensor data for a few frequencies [see Fig. 4(b)], as well as the normalized root mean squared error (NRMSE) at each frequency [see Fig. 4(c)]. The NRSME starts to increase at approximately 20 Hz, which can be explained by the uneven, minimal stroke of the actuator at larger frequencies. This can result in the magnetic block vibrating side to side instead of just moving vertically. Despite this increase, the NRMSE values never exceed 6%. The minimal standard deviation of uncertainty indicates that the sensor output is not affected by environmental changes in temperature and humidity.

B. Comparing the Magnetic Sensing Method to a Capacitive Stretch Sensor

Capacitive stretch sensors are commonly used in soft robotic applications to look at deformations of an actuator or a surface [58]. The stretch sensor has also been successfully used to control a folded HASEL actuator stack [37]. However, optimal performance requires consistent test conditions, dielectric blocks for mitigating noise, and the implementation of filters, which severely limit the sensors' response time. Here, we directly compared the magnetic sensing method with the capacitive stretch sensor in tracking the movement of the folded HASEL actuator. The comparison between the magnetic sensors and the

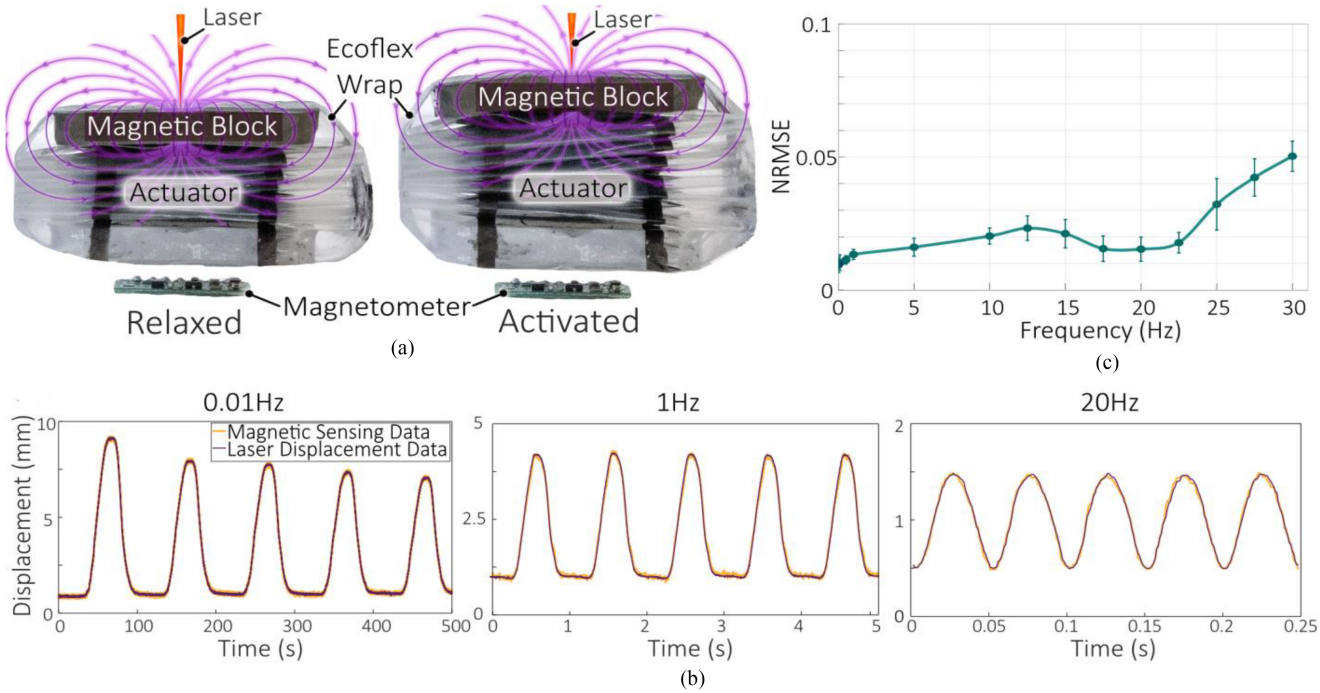

Fig. 4. (a) For each of the frequency tests, a sinusoidal wave was sent to a folded HASEL actuator, which was placed on top of a magnetometer and under a magnetic block – forming a unit. As the actuator moved from a relaxed state to an activated state and back, the laser position sensor measured the change in height by probing the top of the magnetic block. (b) Examples of the mapped magnetometer data superimposed on the laser displacement data. The voltage input to the actuator for each test was a sinewave with an offset on 4 kV and an amplitude of 8 kV; the example plots shown are sine inputs of 0.01, 1, and 20 Hz. For the case of 0.01 Hz, the magnitude of the actuator's displacement decreases overtime mainly due to the charge retention of the actuator [29], [31], [32], [36], but this behavior does not affect the performance of the magnetic sensing method. (c) Average normalized root mean squared error (NRMSE) over forty-five cycles per frequency was recorded, with the error bars representing one standard deviation of uncertainty. The NRMSE never exceeds 6%, even at larger actuation frequencies when the actuator stroke is just a vibration.

capacitive stretch sensors is appropriate due to reasons: they are both embedded sensors that are fully compliant, designed to tolerate high voltage, work well with HASEL actuators, and there are no existing commercial, embedded soft sensors that can be readily used in high-voltage environment.

We wrapped a capacitive stretch sensor around a folded HASEL actuator and a magnetic block [see Fig. 5(a)] to compare the magnetic sensing method with the capacitive stretch sensor. The manufacturing of the capacitive stretch sensor was identical to the sensors used by Johnson et al. [37]. The capacitive sensor has two electrodes made of a conductive, carbon-based silicone; the electrodes sandwich a thin, silicone dielectric layer, which is then wrapped around the actuator. As the actuator changes in height, the capacitive sensor stretches and changes in capacitance. A dielectric shield, which was the same dimension as the magnetic block, was placed under the actuator to separate the capacitive stretch sensor from the actuator, similar to the noise mitigation setup in Johnson et al. [37]. The same 555-timer circuit and second-order low pass filter in Johnson et al. were used to measure the on-time of the output square wave of the 555-timer circuit, which was directly related to the change in capacitance of the capacitive stretch sensors [35]. An MCU measured the on-time of the output square wave in milliseconds in tandem with the change in magnetic flux density in milligauss and the laser displacement data in millimeters. This data was time stamped in microseconds and sent to a computer via serial connection. The input to the actuator was a series of 10 s step functions starting at 2 kV and increasing by 1 to 8 kV. This input, produced by a wave generator, was sent to the actuator through the high-voltage amplifier.

Our sensor significantly outperforms the capacitive stretch sensor in accuracy when measuring the change in height of the actuator. Fig. 5 shows the visibly larger noisy data from the capacitive stretch sensor compared with the magnetometer signal, despite the low-pass filter used for the stretch sensor data. The mean of the residual error $|e|$ (mm) for the magnetic sensor (0.044 mm) is almost eight times smaller than that of the capacitive stretch sensor (0.34 mm), indicating a better fit between the mapped magnetometer data and the laser position data over the folded HASEL actuator displacement range. Unlike the capacitive stretch sensor, the magnetic sensor registers minute changes in displacement when the actuator voltage increases by 1 kV from a 0 kV baseline to 2 kV.

C. Gripper Demonstration With Submillimeter Accuracy

To verify the submillimeter sensing in the displacement range of the HASEL actuator movement using the sensing mechanism, we created a two-finger gripper using two HASEL actuators mounted on a 3D printed, PLA frame (Prusa i3 MK3S+, Prusa) [shown in Fig. 1(b)]. The goal of this demonstration was to sense small differences in the diameter of three tomatoes of similar size (see supplemental video). First, the left and right actuators were individually calibrated using a similar procedure

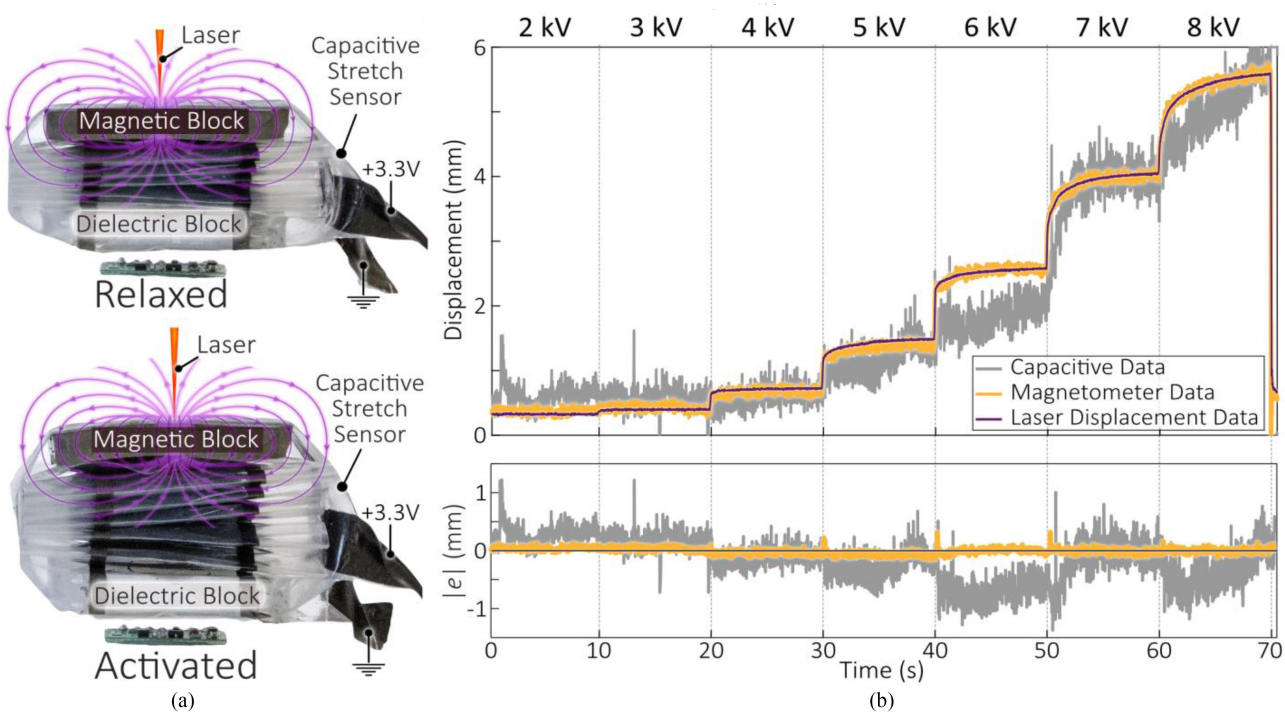

Fig. 5. (a) Capacitive stretch sensor was wrapped around the magnetic block, a dielectric block, and the folded HASEL actuator before being placed on the magnetometer circuit. When activated, the capacitive stretch sensor, magnetic sensing mechanism, and laser position sensor all measured the change in actuator stroke. The capacitive stretch sensor measured this linear change in actuator stroke because it was wrapped around the entire unit and deformed when the unit moved, effectively changing the measured capacitance. (b) Starting at an input of 2 kV, we increased the voltage to the HASEL by 1 kV every 10 s until the input voltage reached 8 kV. The corresponding displacement data measured by each respective sensor highlights the improvement between using the magnetic sensing mechanism compared with the capacitive stretch sensor, where the mean residual error |e| of the magnetic sensing data is eight times smaller than that of the capacitive stretch sensor.

as described in Section III-B. However, instead of mapping the change of height to the change in magnetic flux strength, we mapped the horizontal change in displacement of the actuator, measured by the laser displacement sensor, to the change in magnetic flux strength. To activate the actuators, we supplied an input voltage ramp from 0–8 kV at a rate of 1 kV/s. Two 3rd order polynomial functions were generated to independently determine the displacement for the right actuator, d_{right}, and the displacement for the left actuator, d_{left}. We did not use the same polynomial fit for both actuators due to the slight differences in magnetic block placement, actuator fabrication, and effect of gravity, which added a slight downward tilt to both actuators.

A thin, silicone wrap (Ecoflex, 00–30, Smooth On) was wrapped around the magnetic block and actuator to keep the unit together. By mapping the changes in magnetic flux strength to changes in displacement for the right actuator, d_{right}, and left actuator, d_{left}, we could determine the diameter of an object in between both actuators, d_{meas}

$$d_{\text{meas}} = 45\ \text{mm} - (d_{\text{left}} + d_{\text{right}}) \tag{2}$$

where 45 mm is the distance between the two actuators at rest measured with the laser displacement sensor. Since the placement of the tomato was not guaranteed to be in the center of both actuators, we determined d_{right} and d_{left} based on a change in slope of the left and right displacements. The displacement slopes decrease due to the reaction force generated by the object

TABLE I
COMPARISON OF TOMATO DIAMETER MEASUREMENTS

Tomato	Caliper Measurement (mm)	Sensor Measurement (mm)	e (mm)
1	42.0	42.4	0.4
2	41.9	42.2	0.3
3	42.8	42.9	0.1

that's in contact with the actuator. We also used a caliper (Mitutoyo, Absolute Digimatic Caliper) with a 0.03 mm accuracy rating as a ground truth sensor for comparison. Each of the three tomatoes was measured at the same spots using both the gripper and the caliper; these values and the correlating residual error e are shown in Table I.

While we still achieved submillimeter accuracy in this demonstration, the error values are larger than the expected deviation of ± 0.1 mm shown in Fig. 3(b). As mentioned before, there is a slight downward tilt of both units, which we believe adds some amount of error. Despite a reduction of accuracy, the gripper was still able to distinguish which tomato was the smallest and which tomato was the largest when there was a less than 1 mm difference across the three tomato diameters.

This demonstration shows the ability to safely interact with soft objects, a tomato in this case, in addition to highlighting the accuracy of this sensing mechanism. When activating the units, we supplied an input triangular signal that increased from

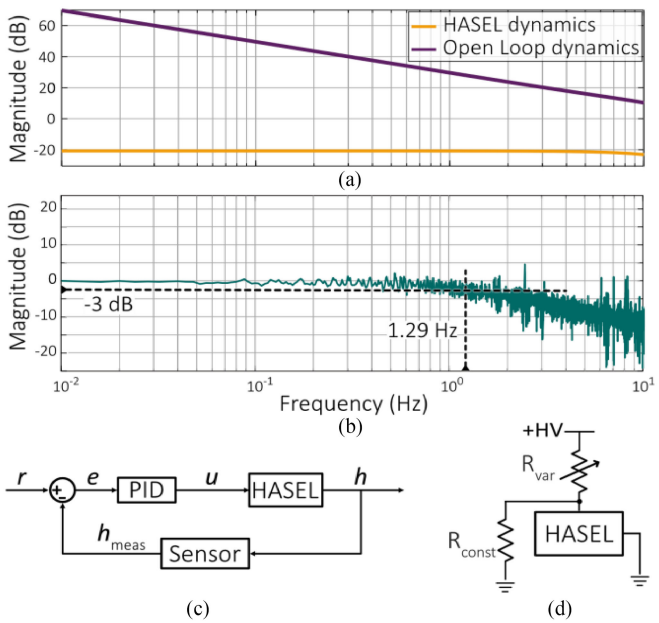

Fig. 6. (a) Magnitude frequency response of the approximated HASEL model (h (mm)/D_{var} (%)) compared with the approximated open-loop system, or the feed-forward loop gain, which includes the PID controller shown in (c). (b) Magnitude frequency response of the closed-loop system. The magnitude compares the output measured height to the input reference signal. Here, the corner frequency (1.29 Hz) is labeled. (c) Block diagram of the closed-loop system using a PID controller and the magnetic sensor to control the HASEL actuator. (d) Basic schematic of the driving circuit.

0 to 8 kV then decreased from 8 to 0 kV. The units continued to expand after initial contact with each tomato because of the input signal (see supplemental video). However, the activated units did not damage the tomato; instead, both units slightly tilted and conformed to the shape of the tomato until the voltage reached the maximum value of 8 kV.

V. Frequency Response of Single-Unit Closed-Loop System

A. System Identification of the Open-Loop System

We validated the sensor in a closed-loop system with a single unit. We performed sinewave-based, dynamic tests with logarithmic chirp input signal to experimentally determine an open-loop model of the actuator. Here, we used the laser position sensor to measure the actuator's true change in height. Instead of using the TREK to provide the variable voltage to the HASEL, we used a driving circuit [see Fig. 6(d)].

The driving circuit design is similar to existing HV switches that are used to control DEAs [59] and HASEL actuators [33]. We customized an optocoupler used on the driving circuit using an infrared LED (L1IZ-0940000000000, Lumileds) and an optodiode (OZ100SG, Voltage Multipliers, Inc.). We used a pair of optocouplers for each actuator: a charging optocoupler with a variable PWM duty cycle D_{var} (%) and a discharging optocoupler with a fixed 45% PWM duty cycle D_{const} (%). The frequency of both PWM inputs was 500 Hz. By changing D_{var} , we can tune the current through the HASEL, thereby controlling the input voltage. We fixed D_{const} to simplify the feedback control to a SISO system. D_{const} was tuned to obtain a reasonable relaxation time, which describes the time it takes for the actuator to reduce in stroke when the input voltage decreases. The driving and discharging optocouplers act like a variable resistor R_{var} and a fixed resistor R_{const} [see Fig. 6(d)].

A high-voltage amplifier (610E, TREK) supplies a constant voltage of 8 kV to the driving circuit. The driving circuit allows for independent control of multiple units in tandem by regulating what fraction of the 8 kV HV line each actuator sees. Using the driving circuit to vary the voltage input during the characterization tests allowed us to use the model and controller designed for a single unit in the larger, multiunit deformable platform described in Section VI.

To vary the voltage to the actuator, $D_{\text{var}}(t)$ is determined by a logarithmic chirp signal generated in MATLAB

$$D_{\text{var}}\ (t) = A \sin\left(2\pi f\left(t\right) t\right) + D_{\text{const}} \tag{3}$$

where A is the amplitude of the input signal (%), t is time (s), and D_{const} is the operating point (45% duty cycle). The frequency $f(t)$ of the input sinewave is determined by

$$f\left(t\right) = f_0 \times \left(\frac{f_1}{f_0}\right)^{\frac{t}{T}} \tag{4}$$

where f_0 and f_1 are the starting and ending frequencies (Hz), respectively, and T is the total time of the chirp signal (s). We fixed the f_0 at 0.01 Hz, the f_1 at 20 Hz, and T at 360 s. We have observed that the maximum stroke of a folded HASEL actuator reduces as frequency increases, until approximately 20 Hz, when the actuator's stroke is minimized to a vibration (see Fig. 4) [35]. Therefore, we mainly focused on the dynamics of the actuator at frequencies below 20 Hz. The amplitude of D_{var} was 30%, making the range of D_{var} equal 15%–75%. This amplitude was experimentally tuned to allow the HASEL to move along its full range of motion at lower frequencies.

We recorded the mapped sensor data, the measured laser position sensor data, and the PWM input at a sampling frequency of 500 Hz to estimate a transfer function that maps the input PWM duty cycle D_{var} (%) to the output HASEL height h (mm). Although we were only interested in the response of the actuator for frequencies below 20 Hz, we used a sampling frequency larger than ten times the end frequency to ensure that we were obtaining enough data for characterization. Based on this frequency response data, we approximated our open-loop single unit as a second-order transfer function

$$P\left(s\right) = \frac{683}{s^2 + 145.5s + 7452}.$$

B. Controller Design and Closed-Loop System Dynamics

While this system is stable, as verified by a Routh–Hurwitz stability test, we wanted to improve the steady-state error and the tracking performance at lower frequencies. We designed a PID controller that increases the gain at lower frequencies to keep the tracking error below 5% up to the 2.86 Hz corner frequency, when the HASEL actuators start to decrease in stroke [see Fig. 6(b)]. This requires the magnitude of the open loop system with the PID controller to be larger than 20 dB up to 2.86 Hz, which we achieve [see Fig. 6(a)]. The integral component of

the controller also insures no steady state error. The discrete-time equations for PID control at time-step k with reference height r, input to the MCU u, measured height h_{meas}, and height error e are

$$e\,[k] \;=\; r\,[k] - h_{\text{meas}}\,[k] \tag{5}$$

$$u\;[k] = \;u\,[k-1] + Ae\,[k] + Be\,[k-1] + Ce\,[k-2]\,. \tag{6}$$

The coefficients on the controller are calculated with

$$A = K_{\text{p}} + \frac{K_{\text{i}}}{2f} + K_{\text{d}} f$$

$$B = -K_{\text{p}} + \frac{K_{\text{i}}}{2f} - 2K_{\text{d}} f$$

$$C = \frac{K_{\text{d}}}{f}$$

$$K_{\text{p}} = 4,061\; K_{\text{i}} = 45,800\; K_{\text{d}} = 0.002$$

where f is the closed-loop frequency (Hz) and K_{p}, K_{i}, and K_{d} are the tuned PID constants. The input u from (5) is the 16-b value which corresponds to D_{var} (%); that is sent to the optocoupler via the MCU. The PID constants are generally large because of the conversion from single-digit actuator heights in mm to five-digit PWM values. However, K_{d} was kept relatively small to prevent overshoot from the controller.

To measure the bandwidth of the closed-loop system, we generated a logarithmic chirp input like the input described in Section V-A. However, to understand the frequency response of the closed-loop system, we examined the frequency response between the laser position sensor data (output) and the reference heights (input). The reference heights $h_{\text{ref}}(t)$ were determined using

$$h_{\text{ref}}\;(t) = \;A \sin\left(2\pi f\,(t)\,t\right) + h_{\text{off}} \tag{7}$$

where $f(t)$ was computed using (3) with $f_0 = 0.01$ Hz, $f_1 = 20$ Hz, and $T = 360$ s. The offset height h_{off} was 3 mm and the amplitude A was 3 mm, resulting in an h_{ref} range of 0–6 mm. Since the HASEL actuation stroke is minimal at frequencies above 20 Hz, we set the closed-loop frequency to $>10\times$ that frequency at 250 Hz. The controller was using Julia v1.6.2, which read the magnetometer and the laser position sensor data from the MCU and outputted PWM inputs to the MCU.

The Bode plot of the closed-loop system is shown in Fig. 6(b), where the input is reference height h_{ref} (mm) and the output is tracked height of the HASEL h (mm). We can achieve at least 70% of the total actuator stroke (-3 dB) at a corner frequency of about 1.29 Hz. This low corner frequency is not surprising when we consider the intrinsic dynamics of the HASEL actuator, which result in a 2.86 Hz corner frequency for the open-loop system (comparing input PWM signal to output height) in Section V-A. However, this indicates that the closed-loop performance will result in higher errors at higher actuation frequencies if the reference height is approaching of the maximum stroke.

VI. Deformable Platform Demonstration for Multisensor, Multiactuator Closed-Loop Control

A. Demonstrating Magnetic Sensing on a Multiunit System

To demonstrate the scalability of a single unit, we created a multiunit soft robotic platform, referred to as the deformable platform. This application showcases the sensor's ability to be used near the electric field generated by the HASEL actuators and highlights the minimal sensor coupling among nearby sensors without impacting the sensor's accuracy or precision. The individual unit control allows for position tracking of the platform's end effector.

B. Design of the Deformable Platform

Our deformable platform is comprised of two segments (top and bottom), with each segment driven by units placed in triradial symmetry (see Fig. 1), like designs of other soft robotic platforms [55], [56], where there is a 120° separation between the placement of each actuator on each segment. The elongation of any of the three actuators causes a pose change of the segment's top surface [see Fig. 4(a)].

The magnetic sensing setup is the same as for the individual unit in Section III; each of the three units has its own magnetic block and sensor. The top of each segment is a 1.5 mm acrylic sheet, and the bottom is the sensor printed circuit board (PCB) described in Section VI-C. HASEL actuators. To match the 120° separation between each unit on both segments, the units are labeled as such on each segment: b_0, b_{120}, b_{240} on the bottom segment and t_0, t_{120}, t_{240} on the top segment; b_0 lies below t_0, b_{120} below t_{120}, and b_{240} below t_{240} [see Fig. 7(a)].

At the boundary between the first and second segments, the magnetic blocks of the bottom segment are near the magnetic sensors of the top segment; however, there is no relative motion between them. Therefore, the magnetic blocks in the bottom segment only impact the base magnetic field measured by the sensors on the top segment. The sensors of the top segment still have full sensitivity to the changes in heights of their respective magnetic blocks.

We used the 4-camera motion capture system (Prime$^{\text{x}}$ 13, OptiTrack) to track the reflective markers used to calibrate the six sensors and measure the end effector's true position during the closed-loop control experiments. During the calibration process described in Section VI-D, six reflective markers were placed in line with the center of each actuator, perpendicular to the edge of the acrylic divider. During the closed-loop experiments, a reflective motion-capture marker was placed on the center point of the top acrylic plate [see Fig. 7(b)]. The marker mount was 60 mm tall, and the spherical marker diameter is 8 mm. We defined the center of the marker as the end effector of the deformable platform and used this to measure the overall error between the end effector position and the reference trajectory.

C. Platform Circuitry

The base of each segment is a PCB that connects the sensors in parallel. These base PCBs connect the three sensors in parallel for each segment and allow for the attachment of additional

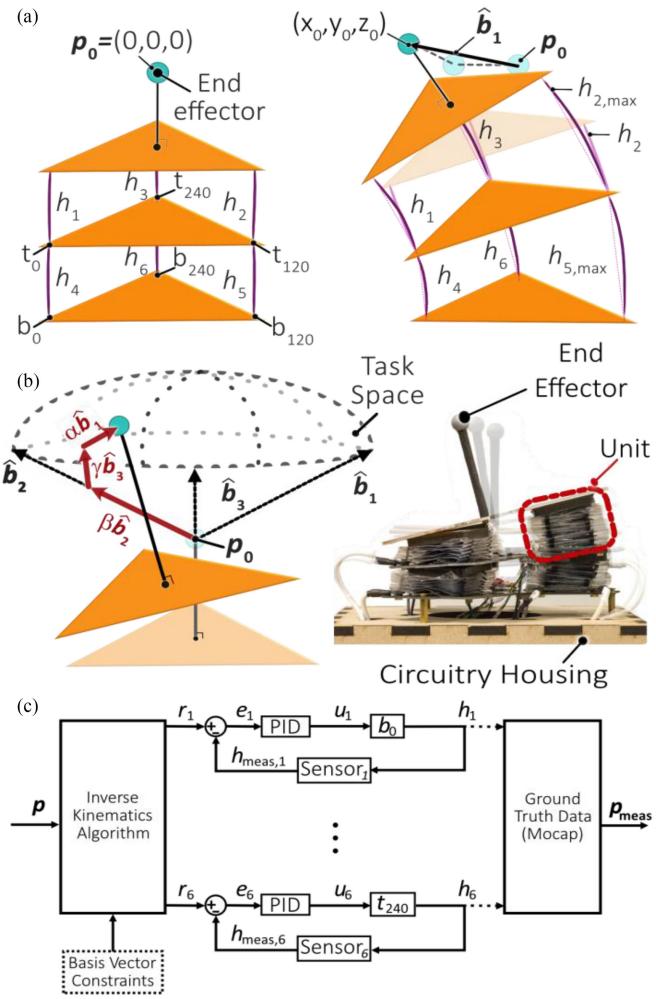

Fig. 7. (a) We experimentally determine three basis vectors $\{\hat{\boldsymbol{b}}_1, \hat{\boldsymbol{b}}_2,\ \hat{\boldsymbol{b}}_3\}$ by determining the change in end effector position $(\boldsymbol{x}_0, \boldsymbol{y}_0, \boldsymbol{z}_0)$ in reference to the end effector's starting position $\boldsymbol{p}_0 = (0, 0, 0)$ when an actuator pair (the 0°, 120°, or 240° position pairs) is at its max stroke. This diagram shows how the basis function $\hat{\boldsymbol{b}}_1$ determined: the vector created by the end effector position when the $\boldsymbol{b}_0$ – $\boldsymbol{t}_0$ pair is fully actuated compared with $\boldsymbol{p}_0$. For the kinematics model, the changes in stroke are assumed to be a linear (dotted line), but the changes in actuator stroke are slightly curved (thick, curved line). Additionally, the position change between the end effector position when $\boldsymbol{b}_0$ is fully actuated and when $\boldsymbol{t}_0$ is fully actuated is assumed to be constant. (b) Corresponding projections of a reference end effector position ($\boldsymbol{\alpha}\hat{\boldsymbol{b}}_1$, $\boldsymbol{\beta}\hat{\boldsymbol{b}}_2$, and $\boldsymbol{\gamma}\hat{\boldsymbol{b}}_3$) are used to determine the six heights ($h_1,\ h_2, h_3, h_4, h_5, h_6$) of the actuators based on the reference end effector position $\boldsymbol{p}$ in $\mathbb{R}^3$. In this example, $\boldsymbol{b}_{120}$ is fully actuated and $\boldsymbol{t}_{120}$ and $\boldsymbol{b}_0$ are partially actuated. Therefore, $\boldsymbol{p}$ can be expressed as a combination of $\alpha\hat{\boldsymbol{b}}_1$ and $\gamma\hat{\boldsymbol{b}}_3$. (c) Inverse kinematic algorithm outputs the reference heights r for all six actuators. The difference between the reference height and the measured height is the error e in mm that feeds into each controller. The six identical PID controllers independently control the heights of the folded HASEL stacks h in mm based on their respective mapped, measured height from the magnetometer output h_{meas} in mm. The resulting end effector position $\boldsymbol{p}_{meas}$ in mm is measured by the motion capture system.

base PCBs. Each base PCB interfaces with the three HASEL actuators on each segment and their respective driving circuits. To prevent arcing between the HV across the actuators and the LV components of the sensing mechanism, the section where the actuators attach to the PCB is isolated from the rest of the PCB.

The bottom base PCB is connected to the same MCU that is sending signals to the six driving circuits. The MCU receives all six sensor signals at 250 Hz as 16-b integers before converting the data to magnetic flux density B_Z in mG. To minimize the large noise spikes in the sensor data, we applied a three-point moving median filter. An ac/dc power supply (SF600, COSAIR) supplies 3.3 V to both base PCBs and to the six driving circuits. The power supply, driving circuits, and MCU were all placed in the circuity housing, shown in Fig. 7(b).

D. Sensor Mapping to Actuator Height

We used the motion capture system to collect the true heights for calibration; this was required to map the change in magnetic flux density to change in actuator height for the deformable platform. The motion capture system tracked the movement of six reflective motion capture markers at 240 Hz during the platform calibration tests. We fed the x-, y-, and z- coordinates of each reflective marker through a set of parametric equations to account for the distance between the actual center of the actuator and the center of the motion capture marker. The baseline height of the bottom segment was approximately 26 mm (from the magnetometer to the magnetic block) and the baseline height of the top segment was approximately 28 mm.

We performed six calibration tests, where each test measured the change in marker position and change in magnetic flux density as the actuator received a series of step inputs: first, input steps from 2 to 8 kV with 1 kV increments and held at 5 s each and second, 0.5 kV steps held at 5 s starting at 8 kV and stepping down to 2 kV. We then fit the magnetometer data to the z-position of the respective marker using the same fitting function from Section III-B. There is some variability in the polynomial coefficients for each unit due to the higher baseline values of the top segment, differences in the structure and fabrication of each actuator and sensor, and error in the placement of the top segment, affecting the weight distribution that the bottom segment experiences.

E. Platform Kinematics and Control

The aim of the deformable platform is to demonstrate integrated sensing between multiple sensors and actuators, so we implemented closed-loop feedback control individually on each of the six units, as outlined in Fig. 7(c). The loop is closed around the height of each HASEL actuator at a closed-loop frequency of 250 Hz. The desired position of the platform end effector, $\boldsymbol{p} = (x, y, z) \in \mathbb{R}^3$, is fed into our custom inverse kinematic solver using MATLAB (R2021a, MathWorks), described in detail in Section VI-E2), which computes the necessary heights for all six actuators $[r_1,\ r_2\ , r_3, r_4, r_5, r_6]$. These heights are sent to the individual controllers in Julia (v1.6.2), effectively moving the end effector to the desired position.

1). Multiunit Closed-Loop Control: We implemented the PID controller derived on the single unit in Section V for each of the six units in the deformable platform [see Fig. 7(c)]. The hardware is identical and each of the six driving circuits receive the same 8 kV input from the TREK. We assumed that the plant transfer function (shown in Section V-A) is the same for all six actuators, despite the actuators' slight discrepancies in maximum strokes, stroke rates, and the difference in weight

distribution between the top and the bottom segments of the platform. All HASEL units are controlled by programs with the same structure and PID constants (5) but different polynomial coefficients corresponding to the appropriate magnetic blocks. The fact that we are utilizing identical hardware and software setup for the multiunit system highlights the independence of the sensor and controller for each unit.

2). Platform Kinematics to Determine Actuator Heights: We approximated the inverse kinematics of the deformable platform to relate the end effector's position $\boldsymbol{p} \in \mathbb{R}^3$ to the scalar heights of the six actuators on the platform. These heights can then be set as the reference height r[k] in (4) for the closed-loop controller of each HASEL/sensor unit. Since our primary focus is to demonstrate the effectiveness of independent and uncoupled multi-HASEL control, we developed an inverse kinematic approach which is much simpler to implement than typical methods [60], [61], but at the cost of end effector tracking accuracy.

Following Jones et al., the kinematics can be represented as two mappings; the task space can be mapped to a configuration space, and the configuration space mapped to the actuator space [60]. We are defining the actuator space as the space where the six actuators can move based on a given reference height input and the task space as the volume where the platform is physically able to track a given reference trajectory. Our configuration space is based on three basis vectors $\{\hat{\boldsymbol{b}}_1, \hat{\boldsymbol{b}}_2,\ \hat{\boldsymbol{b}}_3\}$ and describes the stacked pairs of HASEL actuators: the first basis vector corresponds to the movement of the b_0 HASEL – t_0 HASEL unit pair, the second to the $b_{120} - t_{120}$ pair, and the third to the $b_{240} - t_{240}$ pair. The three basis vectors span S, which is a subset of $\mathbb{R}3$ that describes the task space. A visual representation of $\hat{\boldsymbol{b}}_1$ is illustrated in Fig. 7(a).

The basis vectors were experimentally determined by recording the position of the end effector position using the motion capture system as the three HASEL pairs were independently actuated [see Fig. 7(a)]. For example, when b_0 and t_0 are actuated to their respective maximum heights, and we can measure the change in the end effector position as (x_0, y_0, z_0), then the basis vector $\hat{\boldsymbol{b}}_1$ for the $b_0 - t_0$ pair is

$$\hat{\boldsymbol{b}}_1 = (x_0,\ y_0,\ z_0)\,. \tag{8}$$

Thus, actuating HASEL actuators b_0 and/or t_0 to any height, while keeping the other actuators unactuated, will move the end effector to a position of $\alpha\hat{\boldsymbol{b}}_1$, where α is a scalar value that represents the projection of $\boldsymbol{p}$ on $\hat{\boldsymbol{b}}_1$ [see Fig. 7(b)]. We use the same experimental process of measuring the position change of the end effector when the $b_{120} - t_{120}$ pair and the $b_{240} - t_{240}$ pair are fully actuated to determine $\hat{\boldsymbol{b}}_2$ and $\hat{\boldsymbol{b}}_3$, respectively. Note that we have linearized the end effector path; although the true path has curvature, supported by constant-curvature kinematic models [61], it is negligible enough within our platform to be linearized [see Fig. 7(a)], which greatly simplifies our mappings with some reduction in accuracy.

This allows us to represent the referenced end effector position $\boldsymbol{p}$ as a linear combination of the bases $\{\hat{\boldsymbol{b}}_1, \hat{\boldsymbol{b}}_2, \hat{\boldsymbol{b}}_3\}$:

$$\boldsymbol{p} = (x, y, z) = \alpha\hat{\boldsymbol{b}}_1 + \beta\hat{\boldsymbol{b}}_2 + \gamma\hat{\boldsymbol{b}}_3 \tag{9}$$

TABLE II
HASEL HEIGHTS AS PERCENTAGE OF MAXIMUM FOR α, β, γ

$\mathbf{0 \le \alpha \le 0.5}$	$\mathbf{0 \le \beta \le 0.5}$	$\mathbf{0 \le \gamma \le 0.5}$
t_0: 0%	t_{120}: 0%	t_{240}: 0%
b_0: 100α%	b_{120}: 100β%	b_{240}: 100γ%
$\mathbf{0.5 < \alpha \le 1}$	$\mathbf{0.5 < \beta \le 1}$	$\mathbf{0.5 < \gamma \le 1}$
t_0: 100(α-1)%	t_{120}: 100(β-1)%	t_{240}: 100(γ-1)%
b_0: 100%	b_{120}: 100%	b_{240}: 100%

where α, β, and γ are the scalar parameters corresponding to the reference heights of each respective tri-radial HASEL pair. Any position $\boldsymbol{p}$ within $S \in \mathbb{R}^3$ can be expressed as a sum of these scaled basis vectors. The inverse mapping from the task space S to the configuration space is calculated as follows:

$$\begin{bmatrix} \alpha \\ \beta \\ \gamma \end{bmatrix} = \begin{bmatrix} \hat{\boldsymbol{b}}_1\ \hat{\boldsymbol{b}}_2\ \hat{\boldsymbol{b}}_3 \end{bmatrix}^{-1} \cdot \boldsymbol{p}. \tag{10}$$

The mapping from the configuration space to the actuator space is achieved via piecewise linear functions of the parameters α, β, and γ. Parameter values between 0 and 0.5 are linearly scaled between the min-max heights of the HASEL actuators on the bottom segment of the platform, and values between 0.5 and 1 are scaled between the min-max heights of the HASEL actuators on the top segment in addition to the fully actuated HASEL actuators on the bottom segment. This breakdown is laid out in Table II. Using the combined mappings from the task space to the configuration space (9) and the configuration space to the actuator space (Table II), we can generate a unique solution for the 6 reference HASEL heights $[r_1,\ \ldots, r_6]$ for any given end effector position $\boldsymbol{p}$ [see Fig. 7(b)].

To increase ease of implementation and reduce computational complexity, this inverse kinematic approximation technique uses several simplifications of the real behavior of the platform. As mentioned previously, we linearized the end-effector path during the experimental characterization to form the three basis vectors $\{\hat{\boldsymbol{b}}_1, \hat{\boldsymbol{b}}_2,\ \hat{\boldsymbol{b}}_3\}$. In addition, the superposition of the basis vectors as shown in (8) is not mathematically proven to result in a superposition of the end effector position on the robot.

These assumptions result in small inaccuracies in the inverse kinematic approach. To improve the inverse kinematic accuracy, we additionally scaled α, β, and γ depending on the distance of the end effector position from the origin. This was achieved experimentally by fitting the predicted end effector position to data obtained from the motion capture system. However, this tuning has no impact on the closed-loop performance of each local control loop; it only improves the accuracy of end effector prediction to account for the simplifications that were used.

VII. CLOSED-LOOP CONTROL RESULTS

We demonstrate the ability to perform precise tracking control of a reference trajectory in $\mathbb{R}^3$ by commanding the deformable platform to follow a reference conical helix, where the maximum

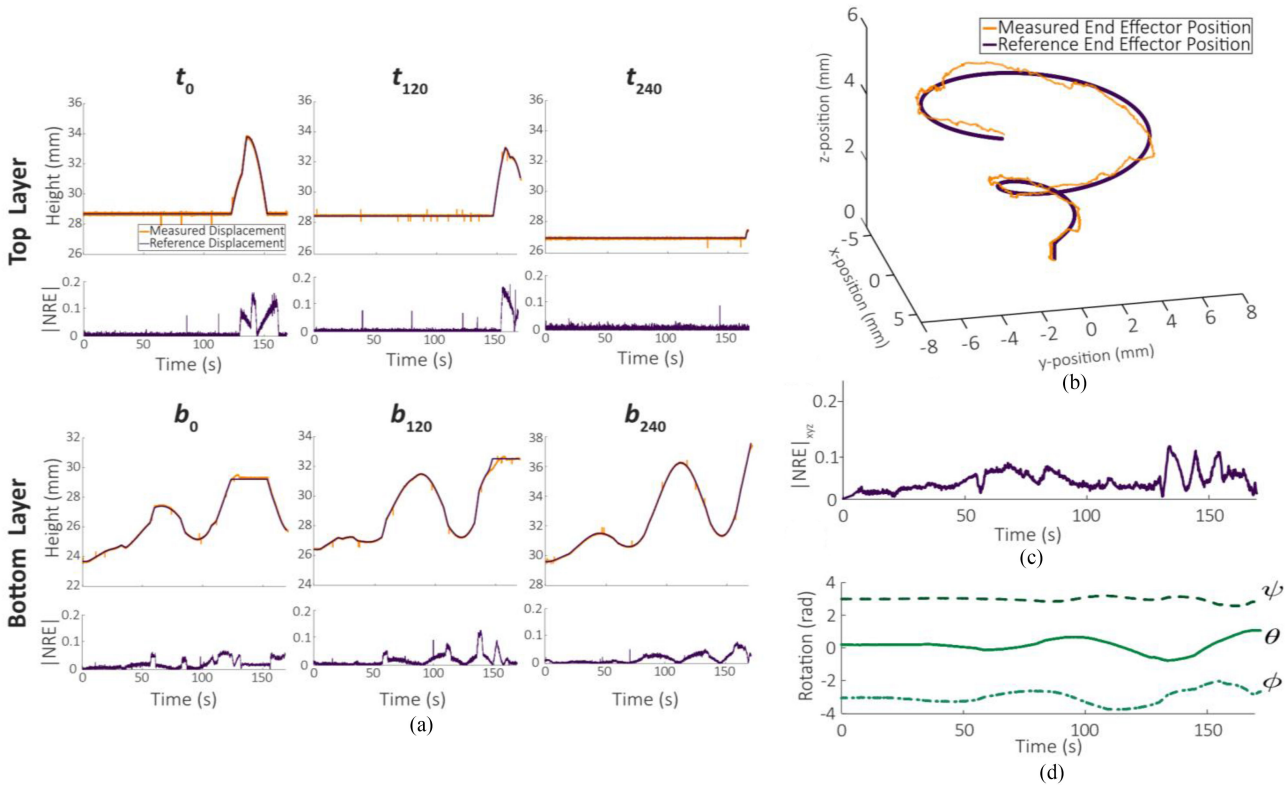

Fig. 8. (a) Measured heights based on motion capture data h_{meas} and the reference heights r for all six actuators, the top actuators positioned at 0°, 120°, and 240° (t_0, t_{120}, t_{240}, respectively) and the bottom actuators positioned at 0°, 120°, and 240° (b_0, b_{120}, b_{240}, respectively). A visual representation of the actuator positioning is shown in Fig. 7(a). There is minimal normalized residual error (NRE) between the measured height, which is the result of controlling each actuator based on the mapped height from the magnetic sensing data and the commanded reference displacement, and the reference height; the NRE is shown below each height subplot. The average normalized residual error (|NRE|) for each of the actuators b_0, b_{120}, b_{240}, t_0, t_{120}, t_{240} are $|NRE|$ = [0.023, 0.021, 0.021, 0.018, 0.015, 0.022], respectively. The mean $|NRE|$ across all six actuators is 0.020, or 2% of the range of the reference heights. (b) Measured p_{meas} and reference end effector positions p start at p_0 = (0,0,0) and move up along a predetermined spiral as each actuator follows the prescribed profile shown in (a). Tracking a reference conical helix demonstrates the control that the platform can accomplish using the magnetic sensing mechanism and a basic control method. (c) Mean of the NRE for the spiral ($|NRE|_{\text{xyz}}$) is 0.043, or 4.3% of the range of the position vector magnitudes. (d) Euler angles that describe the rotational movement of the platform. These values were measured by the motion capture system, which was tracking the end effector marker relative to the system's origin.

range in the x-direction is ∼13 mm, ∼11 mm in the y-direction, and ∼5 mm in the z-direction. The reference position $\boldsymbol{p}$ traces the conical helix that starts at $\boldsymbol{p}$ = (0,0,0) and increases in diameter and height [see Fig. 8(b)]. Despite the assumptions made to simplify the platform kinematics, the deformable platform was able to successfully track both the helix, shown in Fig. 8(b). The error between the reference heights determined from the reference end effector position, $r_n = 1, 2, \ldots, 6$, and the measured heights based on the motion capture data of the tracked markers, $h_n = 1, 2, \ldots, 6$, is minimal [Fig. 8(a)]. The residual error for each unit ($|e_{n\,=\,1,2,..,6}|$) was normalized to the range of the measured height for each individual actuator

$$|\text{NRE}| = \left| \frac{e_{n=1,2,\ldots,6}}{h_{n=1,2,\ldots,6,\text{range}}} \right| = \left| \frac{r_{n=1,2,\ldots,6} - h_{n=1,2,\ldots,6}}{h_{n=1,2,\ldots,6,\text{max}} - h_{n=1,2,\ldots,6,min}} \right|. \quad (11)$$

The average normalized residual error (|NRE|) for actuators $b_0, b_{120}, b_{240}, t_0, t_{120}, t_{240}$ are |NRE| = [0.023 0.021 0.021 0.018 0.015 0.022], respectively, where the overall average |NRE| is 0.020 and the average range of the measured heights is 5.4 mm.

While the NRE between the mapped and reference heights for all six actuators are low, there is some increased variability between the measured end effector position $\boldsymbol{p}_{\mathbf{meas}}$ and the reference end effector position $\boldsymbol{p}$. The normalized residual error ($|\text{NRE}|_{\text{xyz}}$) for the end effector position is

$$|\text{NRE}|_{\text{xyz}} = \frac{\sqrt{\left(\boldsymbol{p}_{\mathbf{x}} - \boldsymbol{p}_{\mathbf{meas,x}}\right)^2 + \left(\boldsymbol{p}_{\mathbf{y}} - \boldsymbol{p}_{\mathbf{meas,y}}\right)^2 + \left(\boldsymbol{p}_{\mathbf{z}} - \boldsymbol{p}_{\mathbf{meas,z}}\right)^2}}{||\boldsymbol{v}||_{\text{max}} - ||\boldsymbol{v}||_{\text{min}}} \quad (12)$$

where

$$||\boldsymbol{v}|| = \sqrt{\boldsymbol{p}_{\mathbf{meas,x}}{}^2 + \boldsymbol{p}_{\mathbf{meas,y}}{}^2 + \boldsymbol{p}_{\mathbf{meas,z}}{}^2}. \quad (13)$$

The mean of the $|\text{NRE}|_{\text{xyz}}$ is 4.3% and the range of the magnitude of the position vectors is 9.3 mm. This increase in error is due to the previously mentioned simplifications of the platform kinematics used when calculating the heights of each actuator based on the desired end effector position. Also, the error for each unit has a compounding effect of the overall error of the end effector position, which results in the increase in NRE seen in Fig. 8.

VIII. Discussion and Conclusion

This article demonstrates the effectiveness of using a magnetic-based sensing mechanism to measure shape deformations of soft electrostatic and electro-hydraulic actuators. This sensing method is simple and elegant to manufacture, scale, and implement, and it proves to be a highly effective method when used with soft electrostatic and electro-hydraulic actuators, specifically HASEL actuators.

While this study focuses on folded HASEL actuators, this sensing mechanism can be used for a multitude of actuators that do not depend on large currents to function. Actuators with a range of motion below 30 mm will benefit from the high accuracy and precision. Since there is an inverse cubic relationship between magnetic flux density and distance, the accuracy and precision decrease as the displacement increases. While this could pose problems for actuators that reach larger strokes than the folded HASEL actuator, there are ways to mitigate this issue, including modifying the thickness of the magnetic block and increasing the concentration of bonded neo-powder.

This sensing mechanism has high accuracy and precision mainly because it is not influenced by HV noise from HASEL actuators, resulting in a clean mapping between change in magnetic flux density and change in actuator height, even at the high end of the HASEL frequency range ($\sim$30 Hz). We were able to use the same cubic mapping function defined in (1) for all the single unit tests and achieve NRMSE values of $<6\%$ [see Fig. 4(c)]. Although the base material of the magnetic block is silicone, changes in the ambient temperature and humidity do not affect the sensor outputs. This can be attributed to physically decoupling the magnetic block from the magnetometer.

When compared with the capacitive stretch sensor previously used to measure the change in HASEL actuator stroke, the magnetic sensing mechanism is significantly more accurate and faster. The mean residual error $|e|$ for the magnetic sensor is approximately eight times less than that of the capacitive stretch sensor. We expected this performance from both sensors since the capacitive sensor is affected by the electric field generated by the HASEL actuator, but the magnetic sensor is not. Fig. 5 shows that the magnetic sensor registers even slight changes in height, unlike the capacitive stretch sensor. This can be attributed to the physical form of each sensor. The capacitive stretch sensor needs to be prestretched to register initial changes in height from a resting height, but the magnetic sensor does not require a prestretch since the sensor and the magnetic component are physically decoupled. Therefore, the magnetic sensor can accurately capture the entire range of displacement of the HASEL actuator, while the capacitive stretch sensor cannot. The high accuracy of the magnetic sensing mechanism is further emphasized in the gripper demonstration. Using this sensing mechanism, we were able to detect submillimeter difference in the diameters of three tomatoes with the worst-case error of only 0.4 mm.

Using an accurate, precise, and fast sensing mechanism to control a soft robot improves the overall performance of the robot. The six-unit deformable platform highlights the ability to independently control multiple units using the magnetic sensing mechanism. For the deformable platform, we assumed the changes in magnetic flux density measured by each sensor were independent of the environment. In reality, the tilt of the platform and the neighboring blocks have a slight influence on the change in magnetic flux density that each magnetometer measures. Accounting for this would improve the accuracy of the mapping and performance of the controller. Furthermore, we acknowledge that, in this work, the calibration process was required for each magnetic block of the platform. Since the calibration step was straightforward and the scope of this work focused on the novel integration of magnetic sensing technique for HASEL actuators, the quality control was not addressed. However, we aim to automate the design and fabrication process for magnetic blocks in the future development of HASEL-based robotic systems.

Despite assuming the magnetic fields are decoupled to allow for independent control, we can maintain a low tracking error for each individual HASEL height [see Fig. 8(a)], where the average normalized error for all six units is 0.020. The assumptions made to simplify the inverse kinematics algorithm increased the overall end effector tracking error. Additionally, the small error in height for each of the six units amplifies the overall end effector tracking error. However, we were not controlling the position of the end effector [see Fig. 7(c)], so this error is not indicative of the performance of the sensing mechanism in a multiunit soft robotic system. This error is only a reflection of the kinematic assumptions we made to calculate the six heights from the end effector position.

In the future, we would like to use this promising sensing mechanism for larger, more advanced, soft robotic platforms. Here, we focused on mapping the change in magnetic flux density in one-dimension to the individual height change of one actuator. To expand on this concept, we could explore using the three-dimensional capabilities of the magnetometer to better understand the soft profile of the actuator with the magnetic block. The decrease in accuracy and precision of the sensing mechanism as height increases can be problematic for actuators with a larger stroke than the folded HASEL actuator used in this study. To negate this issue at larger strokes, we could integrate the magnetic component in the fabrication of the actuator to increase the magnetic flux density closer to the magnetometer. Overall, there is a plethora of applications that can use this sensing mechanism in soft robotic systems due to its high resolution and accuracy, high sampling frequency, ease of manufacturing, and scalability.

Author Disclosure Statement

Mark Rentschler is a co-founder of Aspero Medical, Inc., a start-up company that is focused on commercializing balloon overtube products for use in enteroscopy. Nikolaus Correll is a co-founder and CEO of Robotics Materials, Inc., a start-up company commercializing mobile robotic manipulation.

Acknowledgment

The authors would like to thank A. Gestos and the MIMIC facility for his help in obtaining the XRM images used in this work (MIMIC Facility, RRID:SCR_019307).

REFERENCES

[1] M. T. Tolley et al., "A resilient, untethered soft robot," *Soft Robot.*, vol. 1, no. 3, pp. 213–223, Sep. 2014.

[2] W. Mcmahan et al., "Field trials and testing of the OctArm continuum manipulator," in *Proc. Field Trials Testing OctArm Continuum Manipulator*, 2006, pp. 2336–2341.

[3] D. Rus and M. T. Tolley, "Design, fabrication and control of soft robots," *Nature*, vol. 521, no. 7553, Art. no. 7553, May 2015.

[4] G. M. Whitesides, "Soft robotics," *Angewandte Chemie Int. Ed.*, vol. 57, no. 16, pp. 4258–4273, 2018.

[5] M. Cianchetti, C. Laschi, A. Menciassi, and P. Dario, "Biomedical applications of soft robotics," *Nature Rev. Mater.*, vol. 3, no. 6, pp. 143–153, Jun. 2018.

[6] P. Polygerinos, Z. Wang, K. C. Galloway, R. J. Wood, and C. J. Walsh, "Soft robotic glove for combined assistance and at-home rehabilitation," *Robot. Auton. Syst.*, vol. 73, pp. 135–143, Nov. 2015.

[7] C. Thalman, T. Hertzell, and H. Lee, "Toward a soft robotic ankle-foot orthosis (SR-AFO) exosuit for human locomotion: Preliminary results in late stance plantarflexion assistance," in *Proc. 3rd IEEE Int. Conf. Soft Robot.*, 2020, pp. 801–807.

[8] J.-H. Hsiao, J.-Y. Chang, and C.-M. Cheng, "Soft medical robotics: Clinical and biomedical applications, challenges, and future directions," *Adv. Robot.*, vol. 33, no. 21, pp. 1099–1111, Nov. 2019.

[9] Z. Huichan, K. O'Brien, S. Li, and R. F. Shepherd, "Optoelectronically innervated soft prosthetic hand via stretchable optical waveguides," *Sci. Robot.*, vol. 1, no. 1, Dec. 2016, Art. no. eaai7529.

[10] Z. Yoder et al., "Design of a high-speed prosthetic finger driven by Peano-HASEL actuators," *Front. Robot. AI*, vol. 7, 2020, Art. no. 586216.

[11] E. T. Roche et al., "Soft robotic sleeve supports heart function," *Sci. Transl. Med.*, vol. 9, no. 373, Jan. 2017, Art. no. eaaf3925.

[12] M. A. Horvath et al., "An organosynthetic soft robotic respiratory simulator," *APL Bioeng.*, vol. 4, no. 2, Jun. 2020, Art. no. 026108.

[13] J. Gafford et al., "Shape deposition manufacturing of a soft, atraumatic, and deployable surgical grasper," *J. Mech. Robot.*, vol. 7, May 2015, Art. no. 021006.

[14] J. Shintake, V. Cacucciolo, D. Floreano, and H. Shea, "Soft robotic grippers," *Adv. Mater.*, vol. 30, no. 29, 2018, Art. no. 1707035.

[15] R. L. Truby, L. Chin, and D. Rus, "A recipe for electrically-driven soft robots via 3D printed handed shearing auxetics," *IEEE Robot. Automat. Lett.*, vol. 6, no. 2, pp. 795–802, Apr. 2021.

[16] N. D. Naclerio, C. M. Hubicki, Y. O. Aydin, D. I. Goldman, and E. W. Hawkes, "Soft robotic burrowing device with tip-extension and granular fluidization," in *Proc. IEEE/RSJ Int. Conf. Intell. Robots Syst.*, 2018, pp. 5918–5923.

[17] A. S. Chen, H. Zhu, Y. Li, L. Hu, and S. Bergbreiter, "A paper-based electrostatic zipper actuator for printable robots," in *Proc. IEEE Int. Conf. Robot. Automat.*, 2014, pp. 5038–5043.

[18] X. Yan, M. Qi, and L. Lin, "Self-lifting artificial insect wings via electrostatic flapping actuators," in *Proc. 28th IEEE Int. Conf. Micro Electro Mech. Syst.*, 2015, pp. 22–25.

[19] I. D. Sîrbu et al., "Electrostatic bellow muscle actuators and energy harvesters that stack up," *Sci. Robot.*, vol. 6, Feb. 2021, Art. no. eaaz5796.

[20] J. Kedzierski and E. Holihan, "Linear and rotational microhydraulic actuators driven by electrowetting," *Sci. Robot.*, vol. 3, Sep. 2018, Art. no. eaat5643.

[21] R. K. Katzschmann, A. D. Marchese, and D. Rus, "Hydraulic autonomous soft robotic fish for 3D swimming," in *Proc. Exp. Robot.: 14th Int. Symp. Exp. Robot.*, M. A. Hsieh, O. Khatib, and V. Kumar, Eds. Cham, Switzerland: Springer, 2016, pp. 405–420.

[22] Y. Mori et al., "Feedback control of a pneumatically driven soft finger using a photoelastic polyurethane bending sensor," *Adv. Robot.*, vol. 35, no. 12, pp. 1–16, Apr. 2021.

[23] J. Walker et al., "Soft robotics: A review of recent developments of pneumatic soft actuators," *Actuators*, vol. 9, no. 1, pp. 3–29, Mar. 2020.

[24] J. Wirekoh, L. Valle, N. Pol, and Y.-L. Park, "Sensorized, flat, pneumatic artificial muscle embedded with biomimetic microfluidic sensors for proprioceptive feedback," *Soft Robot.*, vol. 6, no. 6, pp. 768–777, 2019.

[25] Y. Alapan, A. C. Karacakol, S. N. Guzelhan, I. Isik, and M. Sitti, "Reprogrammable shape morphing of magnetic soft machines," *Sci. Adv.*, vol. 6, Sep. 2020, Art. no. eabc6414.

[26] A. Koivikko, D.-M. Drotlef, M. Sitti, and V. Sariola, "Magnetically switchable soft suction grippers," *Extreme Mech. Lett.*, vol. 44, Apr. 2021, Art. no. 101263.

[27] M. Russo, J. Barrientos-Diez, and D. Axinte, "A kinematic coupling mechanism with binary electromagnetic actuators for high-precision positioning," *IEEE/ASME Trans. Mechatronics*, vol. 27, no. 2, pp. 892–903, Apr. 2022.

[28] N. A. Mansour, B. Shin, B. Ryu, and Y. Kim, "Development of a novel miniaturized electromagnetic actuator for a modular serial manipulator," *Actuators*, vol. 10, no. 1, pp. 14–27, Jan. 2021.

[29] J. Mersch, M. Bruns, A. Nocke, C. Cherif, and G. Gerlach, "High-displacement, fiber-reinforced shape memory alloy soft actuator with integrated sensors and its equivalent network model," *Adv. Intell. Syst.*, vol. 7, 2021, Art. no. 2000221.

[30] M. Cianchetti, "Fundamentals on the use of shape memory alloys in soft robotics," in *Interdisciplinary Mechatronics*. Hoboken, NJ, USA: Wiley, 2013, pp. 227–254.

[31] E. Acome et al., "Hydraulically amplified self-healing electrostatic actuators with muscle-like performance," *Science*, vol. 359, no. 6371, pp. 61–65, Jan. 2018.

[32] P. Rothemund, N. Kellaris, S. K. Mitchell, E. Acome, and C. Keplinger, "HASEL artificial muscles for a new generation of lifelike robots—Recent progress and future opportunities," *Adv. Mater.*, vol. 33, 2021, Art. no. 2003375.

[33] S. K. Mitchell et al., "An easy-to-implement toolkit to create versatile and high-performance HASEL actuators for untethered soft robots," *Adv. Sci.*, vol. 6, no. 14, 2019, Art. no. 1900178.

[34] N. Kellaris, V. G. Venkata, G. M. Smith, S. K. Mitchell, and C. Keplinger, "Peano-HASEL actuators: Muscle-mimetic, electrohydraulic transducers that linearly contract on activation," *Sci. Robot.*, vol. 3, no. 14, Jan. 2018, Art. no. eaar3276.

[35] N. Farrow and N. Correll, "A soft pneumatic actuator that can sense grasp and touch," in *Proc. IEEE/RSJ Int. Conf. Intell. Robots Syst.*, 2015, pp. 2317–2323.

[36] S. A. Manzano, P. Xu, K. Ly, R. Shepherd, and N. Correll, "High-bandwidth nonlinear control for soft actuators with recursive network models," in *Experimental Robotics*, Cham, 2021, pp. 589–599, doi: 10.1007/978-3-030-71151-1_52.

[37] B. K. Johnson et al., "Identification and control of a nonlinear soft actuator and sensor system," *IEEE Robot. Automat. Lett.*, vol. 5, no. 3, pp. 3783–3790, Jul. 2020.

[38] S. Benjamin et al., "Electronic skins and machine learning for intelligent soft robots," *Sci. Robot.*, vol. 5, no. 41, Apr. 2020, Art. no. eaaz9239.

[39] T. T. George, S. Benjamin, L. Cecilia, and T. M. Thomas, "Soft robot perception using embedded soft sensors and recurrent neural networks," *Sci. Robot.*, vol. 4, no. 26, Jan. 2019, Art. no. eaav1488.

[40] K. Ly et al., "Miniaturized circuitry for capacitive self-sensing and closed-loop control of soft electrostatic transducers," *Soft Robot.*, vol. 8, no. 6, pp. 673–686, Dec. 2021, doi: 10.1089/soro.2020.0048.

[41] C. Schunk et al., "System identification and closed-loop control of a hydraulically amplified self-healing electrostatic (HASEL) actuator," in *Proc. IEEE/RSJ Int. Conf. Intell. Robots Syst.*, 2018, pp. 6417–6423.

[42] J. Lenz and S. Edelstein, "Magnetic sensors and their applications," *IEEE Sens. J.*, vol. 6, no. 3, pp. 631–649, Jun. 2006.

[43] J. J. Clark, "A magnetic field based compliance matching sensor for high resolution, high compliance tactile sensing," in *Proc. IEEE Int. Conf. Robot. Automat.*, 1988, vol. 2, pp. 772–777.

[44] T. Paulino et al., "Low-cost 3-axis soft tactile sensors for the human-friendly robot Vizzy," in *Proc. IEEE Int. Conf. Robot. Automat.*, 2017, pp. 966–971.

[45] M. H. bin Rosle, R. Kojima, Z. Wang, and S. Hirai, "Soft fingertip with tactile sensation for detecting grasping orientation of thin object," in *Proc. IEEE Int. Conf. Robot. Biomimetics*, 2018, pp. 1304–1309.

[46] L. Jamone, L. Natale, G. Metta, and G. Sandini, "Highly sensitive soft tactile sensors for an anthropomorphic robotic hand," *IEEE Sens. J.*, vol. 15, no. 8, pp. 4226–4233, Aug. 2015.

[47] H. Wang et al., "Design methodology for magnetic field-based soft tri-axis tactile sensors," *Sensors*, vol. 16, no. 9, Aug. 2016, Art. no. 1356.

[48] Y. Yan et al., "Soft magnetic skin for super-resolution tactile sensing with force self-decoupling," *Sci. Robot.*, vol. 6, Feb. 2021.

[49] T. Hellebrekers, O. Kroemer, and C. Majidi, "Soft magnetic skin for continuous deformation sensing," *Adv. Intell. Syst.*, vol. 1, no. 4, 2019, Art. no. 1900025.

[50] A. S. Almansouri et al., "An imperceptible magnetic skin," *Adv. Mater. Technol.*, vol. 4, no. 10, 2019, Art. no. 1900493.

[51] M. Luo et al., "Toward modular soft robotics: Proprioceptive curvature sensing and sliding-mode control of soft bidirectional bending modules," *Soft Robot.*, vol. 4, no. 2, pp. 117–125, Feb. 2017.

[52] H. Mirzanejad and M. Agheli, "Soft force sensor made of magnetic powder blended with silicone rubber," *Sens. Actuators Phys.*, vol. 293, pp. 108–118, Jul. 2019.
[53] S. Wu, W. Hu, Q. Ze, M. Sitti, and R. Zhao, "Multifunctional magnetic soft composites: A review," *Multifunctional Mater.*, vol. 3, no. 4, Dec. 2020, Art. no. 042003.
[54] Y. Huang, M. Gou, P. Zhang, X. Wang, H. Xie, and X. Sheng, "A novel method for detecting joint angles based on inertial and magnetic sensors," in *Proc. 25th Int. Conf. Mechatronics Mach. Vis. Pract.*, 2018, pp. 1–6.
[55] P. Rothemund, S. Kirkman, and C. Keplinger, "Dynamics of electrohydraulic soft actuators," *Proc. Nat. Acad. Sci.*, vol. 117, no. 28, pp. 16207–16213, Jul. 2020.
[56] E. P. Furlani, "Chapter 2—Review of Maxwell's equations," in *Permanent Magnet and Electromechanical Devices*, E. P. Furlani, Ed. San Diego, CA, USA: Academic, 2001, pp. 73–95.
[57] H. Wang, M. Totaro, and L. Beccai, "Toward perceptive soft robots: Progress and challenges," *Adv. Sci.*, vol. 5, no. 9, Jul. 2018, Art. no. 1800541.
[58] A. Tairych and I. A. Anderson, "Capacitive stretch sensing for robotic skins," *Soft Robot.*, vol. 6, no. 3, pp. 389–398, May 2019.
[59] S. Schlatter, P. Illenberger, and S. Rosset, "Peta-pico-Voltron: An open-source high voltage power supply," *HardwareX*, vol. 4, Oct. 2018, Art. no. e00039.
[60] K. Cao, R. Kang, D. T. Branson III, S. Geng, Z. Song, and J. S. Dai, "Workspace analysis of tendon-driven continuum robots based on mechanical interference identification," *J. Mech. Des.*, vol. 139, no. 6, Apr. 2017, Art. no. 062303.
[61] A. Chawla, C. Frazelle, and I. Walker, "A comparison of constant curvature forward kinematics for multisection continuum manipulators," in *Proc. 2nd IEEE Int. Conf. Robot. Comput.*, 2018, pp. 217–223.

Vani Sundaram received the B.S. degree in mechanical engineering from the University of Pittsburgh, Pittsburgh, PA, USA, in 2018, and the M.S. degree in mechanical engineering from the University of Colorado Boulder, Boulder, CO, USA, in 2022, where she is currently working toward the graduate degree.

She is currently with the University of Colorado Boulder, where she is Developing, Validating, and Implementing Sensing and Control Methods for Scalable Soft Robotic Systems. She is also interning with Fundamental AI Research (FAIR), Pittsburgh, PA, USA. She is the recipient of the National Science Foundation Graduate Research Fellowship, Achievement Rewards for College Scientists, and Massachusetts Institute of Technology's Rising Star awards. She is interested in using soft robotic systems to improve prosthetics and orthotics.

Khoi Ly received the B.S. degree in mechanical engineering from Texas Tech University, Lubbock, TX, USA, in 2017, and the M.S. and Ph.D. degrees in mechanical engineering from the University of Colorado Boulder, Boulder, CO, USA, in 2019 and 2021, respectively.

He is currently a Postdoctoral Research Associate with the Organic Robotics Laboratory, Department of Mechanical Engineering, Cornell University, Ithaca, NY, USA. He is interested in developing organic robotic systems that are inspired by nature to bridge the gap between conventional robotics and biological systems.

Brian K. Johnson received the B.S. degree in mechanical engineering from Cornell University, Ithaca, NY, USA, in 2017, and the M.S. and Ph.D. degrees in mechanical engineering from the University of Colorado Boulder, Boulder, CO, USA, in 2020 and 2022, respectively.

He was a National Science Foundation Graduate Research Fellow with the Advanced Medical Technologies Laboratory, University of Colorado Boulder. He is interested in the integration and control of soft actuator and sensor systems to create multifunctional robots

Mantas Naris received the B.S. degree in biomedical engineering from Case Western Reserve University, Cleveland, OH, USA, in 2017. He is currently working toward the graduate degree with the University of Colorado Boulder, Boulder, CO, USA, where he has been working with Dr. J. Sean Humbert at the Bioinspired Perception and Robotics Laboratory.

He is interested in controls engineering research for bioinspired robotics, soft robotics, and actuator-rich systems.

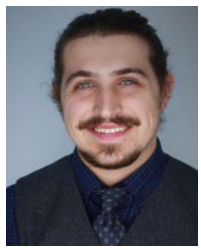

Maxwell P. Anderson received the B.S. degree (with Hons.) in mechanical engineering from the University of Colorado Boulder, Boulder, Boulder, CO, USA, in 2022. He will begin working toward the M.S. degree in mechanical engineering with the University of Colorado Boulder, where he will be focusing on robotics and controls engineering.

He is currently interning with Northwestern Research Associates Inc., as a Student Researcher Working on Micrometeorology and Monin-Obukohv Simularity Theory. He worked at the Advanced Medical Technologies Laboratory as an Undergraduate Assistant, where he received two grants from the Biological Sciences Initiative and a fellowship award from the Discovery Learning Apprenticeship program.

James Sean Humbert received the B.S. degree from the University of California Davis, Davis, CA, USA, in 1997, and the M.S. and Ph.D. degrees from California Institute of Technology, Pasadena, CA, USA, in 1999 and 2005, respectively, all in mechanical engineering.

He is currently the Denver Business Challenge Professor with the Department of Mechanical Engineering, University of Colorado Boulder, Boulder, CO, USA. His fundamental training is in control and dynamical systems, and his main research areas are autonomy, flight dynamics, estimation, control applied to aerospace vehicles and perception, reduction, and feedback principles in biology.

Dr. Humbert is a core member of the Board on Army RDT&E, Systems Acquisition and Logistics (BARSL) and is an AIAA Associate Fellow. He is the recipient of the AIAA National Capital Section Hal Andrews Young Scientist/Engineer Award and an ARO Young Investigator Award.

Nikolaus Correll (Senior Member, IEEE) received the Diploma in electrical engineering from the Eidgenössische Technische Hochschule (ETH) Zürich, Zürich, Switzerland, in 2003, and the Ph.D. degree in computer science from the École Polytechnique Fédérale de Lausanne (EPFL), Lausanne, Switzerland, in 2007.

He was a Postdoctoral Associate with the Massachusetts Institute of Technology's (MIT) Computer Science and Artificial Intelligence Laboratory till 2009. He is currently an Associate Professor of Computer Science with the University of Colorado Boulder, Boulder, CO, USA. His research interests are in robotic materials and robotic manipulation.

Mark Rentschler (Senior Member, IEEE) received the B.S. degree in mechanical engineering from the University of Nebraska, Lincoln, NE, USA, in 2001, the M.S. degree in mechanical engineering from the Massachusetts Institute of Technology (MIT), Cambridge, MA, USA, in 2003, where he was a National Defense Science and Engineering Graduate (NDSEG) Fellow, and the Ph.D. degree in biomedical engineering from the University of Nebraska, in 2006.

He is currently a Professor and Sylvia Norviel Cancer Research Faculty Fellow in mechanical engineering with the University of Colorado Boulder, Boulder, CO, USA. He also holds a secondary appointment with the Department of Surgery, University of Colorado Anschutz Medical Campus, Aurora, CO, USA. His research interests are in medical devices and surgical robotics.

Dr. Rentschler is also a fellow of ASME and a Senior Member of the National Academy of Inventors.